Available online at www.sciencedirect.com
ScienceDirect
Journal of the Mechanics and Physics of Solids 56 (2008) 2019–2035
JOURNAL OF THE MECHANICS AND PHYSICS OF SOLIDS
www.elsevier.com/locate/jmps

A self-consistent boundary element, parametric dislocation dynamics formulation of plastic flow in finite volumes

Jaafar A. El-Awady[a,*], S. Bulent Biner[b], Nasr M. Ghoniem[a]

[a]*Mechanical and Aerospace Engineering Department, University of California, Los Angeles (UCLA), Los Angeles, CA 90095-1597, USA*
[b]*Ames Laboratory, Materials and Engineering Physics, Iowa State University, Ames, IA 50011, USA*

Received 3 April 2006; received in revised form 5 September 2007; accepted 7 November 2007

Abstract

We present a self-consistent formulation of 3-D parametric dislocation dynamics (PDD) with the boundary element method (BEM) to describe dislocation motion, and hence microscopic plastic flow in finite volumes. We develop quantitative measures of the accuracy and convergence of the method by considering a comparison with known analytical solutions. It is shown that the method displays absolute convergence with increasing the number of quadrature points on the dislocation loop and the surface mesh density. The error in the image force on a screw dislocation approaching a free surface is shown to increase as the dislocation approaches the surface, but is nevertheless controllable. For example, at a distance of one lattice parameter from the surface, the relative error is less than 5% for a surface mesh with an element size of 1000×2000 (in units of lattice parameter), and 64 quadrature points. The Eshelby twist angle in a finite-length cylinder containing a coaxial screw dislocation is also used to benchmark the method. Finally, large scale 3-D simulation results of single slip behavior in cylindrical microcrystals are presented. Plastic flow characteristics and the stress–strain behavior of cylindrical microcrystals under compression are shown to be in agreement with experimental observations. It is shown that the mean length of dislocations trapped at the surface is the dominant factor in determining the size effects on hardening of single crystals. The influence of surface image fields on the flow stress is finally explored. It is shown that the flow stress is reduced by as much as 20% for small single crystals of size less than 0.15 μm.

Keywords: Dislocations; Image field; Boundary integral equations; Size effects; Microcrystals

1. Introduction

Understanding dislocation interaction with free and internal surfaces (e.g. grain boundaries, precipitate surfaces, twin boundaries, voids, bubbles, and cracks) is essential in a wide range of applications, such as fatigue crack nucleation (Basinski et al., 1983; Mughrabi, 1992), thin film deformation (Arzt et al., 2001), and size effects on small sample plasticity (Greer et al., 2005; Dimiduk et al., 2005). Discrete dislocation dynamics (DDD) has been developed to simulate plastic deformation at the meso-scale by direct numerical solution of the equations of motion for dislocation ensembles. The approach has been successfully used in many applications at the nano- and microscales (e.g. Kubin et al., 1992; Zbib et al., 1998; Schwarz, 1999; Ghoniem

*Corresponding author. Tel.: +1 310 351 7997; fax: +1 310 206 4830.
E-mail address: jelawady@ucla.edu (J.A. El-Awady).

0022-5096/$ - see front matter © 2007 Elsevier Ltd. All rights reserved.
doi:10.1016/j.jmps.2007.11.002

et al., 2000). However, the majority of these approaches are for bulk crystals, with a few exceptions that consider the influence of free or internal surfaces (e.g. Fivel et al., 1996; Schwarz, 1999; Kukta and Freund, 1998; Ghoniem and Sun, 1999; Khraishi et al., 2001; Martinez and Ghoniem, 2002; Weygand et al., 2002). Careful assessments of the accuracy associated with these numerical methods would be helpful, especially because of the singular behavior of the elastic field of dislocations at free surfaces and interfaces.

Elasticity methods to account for the influence of free surfaces or interfaces may be grouped into the following categories:

1. *Superposition methods*, where regular solutions obtained by numerical methods (e.g. the finite element, boundary element Weygand et al., 2002; Martinez and Ghoniem, 2002, or the Boussinesque point force solution on a free surface, Verdier et al., 1998) are superposed on singular solutions for dislocations in infinite media to satisfy traction equilibrium at the free surface.
2. *Approximation techniques*, based on Lothe's solution (Lothe et al., 1982; Schwarz, 1999), or by assuming that interfaces are rigid (von Blanckenhagen et al., 2001).
3. *The surface dislocation method*, where a surface dislocation loop distribution is determined so as to satisfy interfacial or free surface traction conditions at collocation points (Khraishi et al., 2001).
4. *Elasticity methods*, based on solutions of a dislocation segment near a free surface (Gosling and Willis, 1994; Fivel et al., 1996).

The boundary element method (BEM) belongs to the first category; but it is advantageous over the finite element method (FEM) for a number of reasons. In the BEM approach, discretization takes place only on the surface rather than throughout the entire volume, with an obvious reduction in the number of degrees of freedom and in computational requirements. Stresses and displacements at interior points are calculated more accurately in the BEM, because all field variables are discretized on the surface and no further approximation is imposed on the solution at interior points. Furthermore, in the FEM, interpolation of field variables is required at locations not coinciding with Gaussian integration points. On the other hand, stresses and displacements in the BEM are calculated directly at the point of interest without the need for interpolation. One additional and significant advantage of the BEM is associated with modelling the evolution of surfaces as a result of step, ledge, and crack formation during plastic deformation. Surface nodes need only be re-discretized every now and then for a prescribed level of accuracy. This type of flexibility is very difficult to attain with other methods of solution.

The governing differential equations for field quantities in the BEM are transformed into integral identities over the boundary (surface). These integrals are numerically integrated over the entire surface by dividing it into surface elements. With specified displacement or traction boundary conditions, a system of linear algebraic equations is obtained, and the system can be solved with methods of linear algebra.

In this work, we present an implementation of the BEM method in dislocation dynamics simulations to incorporate the influence of free and internal interfaces on dislocation motion. First, a brief outline of the theoretical framework of the parametric dislocation dynamics (PDD) and the BEM are given in Section 2. In Section 3, we develop qualitative measures for the accuracy and convergence of the method by considering a comparison with two known analytical solutions. The interaction of a screw dislocation with a free surface, as obtained from the PDD-BEM method for different mesh densities on a free surface, is compared with the analytical solution. Then the twist angle produced in a cylinder containing a coaxial screw dislocation is compared with analytical formulas developed by Eshelby.

In Section 4, the developed PDD-BEM method is utilized to examine the size effects of single-slip behavior in cylindrical microcrystals. The setup of computer simulations for experiments on compression of micropillars is explained in Section 4.1, and 3-D simulation results are presented and discussed in Section 4.2. In addition, influence of the image field on the microstructure and flow stress influence of microcrystals is explored. Finally, conclusions and a discussion are given in Section 5.

2. Consistency of the PDD and the BEMs

The elastic field, forces, and motion of dislocation loops in an infinite medium are computed using the PDD methodology, developed by Ghoniem and Sun (1999) and Ghoniem et al. (2000). Detailed information about

the method can be found elsewhere, but for the completeness of the current work we summarize related information. In this approach, any 3-D dislocation loop of an arbitrary shape is discretized into N_{seg} curved parametric segments. The configuration of each segment, j, is completely defined by choosing a set of generalized coordinates q_{ik}^{j} and corresponding shape functions $\mathscr{C}_i(\omega)$ as follows:

$$x_k^{(\beta)}(\omega) = \sum_i \mathscr{C}_i(\omega) q_{ik}^{(\beta)}, \tag{1}$$

where $x_k^{(\beta)}$ is the Cartesian coordinates of a point on segment β, and ω is a parameter that defines the location of the point on the segment and is in the interval $0 \leqslant \omega \leqslant 1$. For the present study, we employ cubic spline segments and thus the generalized coordinates are the position and tangent vectors associated with the beginning and end of the segments (i.e. at $\omega = 0$ and 1, respectively). Following Ghoniem and Sun (1999), the stress field tensor at any point due to N_{loop} dislocation loops that are divided into N_{seg} segment can be written as a fast numerical sum over: quadrature points ($1 \leqslant \gamma \leqslant Q_{\max}$) associated with weight factors (w_α), loop segments ($1 \leqslant \alpha \leqslant N_{\text{seg}}$), and number of dislocation loops ($1 \leqslant \beta \leqslant N_{\text{loop}}$), as follows:

$$\sigma_{ij} = \frac{\mu}{4\pi} \sum_{\gamma=1}^{N_{\text{loop}}} \sum_{\beta=1}^{N_{\text{seg}}} \sum_{\alpha=1}^{Q_{\max}} b_n w_\alpha \left[\frac{1}{2} R_{,mpp} (\varepsilon_{jmn} x_{i,\omega}^{(\beta)} + \varepsilon_{imn} x_{j,\omega}^{(\beta)}) + \frac{1}{1-v} \varepsilon_{kmn} (R_{,ijm} - \delta_{ij} R_{,ppm}) x_{k,\omega}^{(\beta)} \right], \tag{2}$$

where ε_{ijk} is the permutation tensor, μ is the shear modulus, v is Poisson's ratio, b_n is the components of the Burgers vector $\mathbf{b}$, $x_{k,\omega}^{(\beta)}$ are the parametric derivatives of the Cartesian components which describe the 3-D dislocation segment β as a function of the parameter ω, and $\mathbf{R}$ is the radius vector that connects a source point $x_k^{(\beta)}$ on a dislocation loop to the field point at which the stress is being evaluated, and has Cartesian components R_i, successive partial derivatives $R_{,ijk\ldots}$ and magnitude R.

Following the superposition method developed by Van der Giessen, Needleman and co-workers (Van der Giessen and Needleman, 1995; Weygand et al., 2002) to introduce boundary conditions in DDD, the total stress and displacement fields are given as

$$\begin{aligned} \sigma_{ij} &= \widetilde{\sigma_{ij}} + \widehat{\sigma_{ij}}, \\ u_{ij} &= \widetilde{u_{ij}} + \widehat{u_{ij}}, \end{aligned} \tag{3}$$

where the ($\sim$) fields are the elastic fields in an infinite medium resulting from all dislocation loops given by Eq. (2), while the ($\wedge$) fields are the *image fields* that enforce boundary conditions. To evaluate the *image fields* due to external or internal surfaces, the following four steps need to be performed. First, the elastic stress field in an infinite medium resulting from all dislocation loops is evaluated. The tractions at the surfaces of the finite crystal due to this stress field are then determined, reversed and placed on the surface as traction boundary conditions. These traction boundary conditions in addition to any imposed displacement constrains are employed in BEM to calculate all other unknown surface tractions and displacements. Finally, the image stress field is calculated, and the result is superimposed as indicated in Eq. (3).

The boundary integral equation (BIE) for the response at any point P due to displacements and tractions applied at point Q is developed using the reciprocal theory and the fundamental Kelvin problem solutions. The BIE is given as (Becker, 1992)

$$c_{ij}(P) u_j(P) = \int_S U_{ij}(P,Q) t_j(Q)\, \mathrm{d}S - \int_S T_{ij}(P,Q) u_j(Q)\, \mathrm{d}S, \tag{4}$$

where S is the boundary, c_{ij} is a coefficient matrix, which in general is computed by applying rigid body motion, and U_{ij} and T_{ij} are the displacement and traction kernel, respectively.

Eq. (4) is solved over any closed boundary by dividing the surface into boundary elements, where the integration is obtained numerically over each element after enforcing the boundary conditions. Once all the surface displacements and tractions are obtained by solving the above BIE, the image field at any dislocation point P can then be easily computed for any material with elastic constants C_{ijkl} as follows:

$$\sigma_{ij} = \int_S G_{ijk}(P,Q) t_k(Q)\, \mathrm{d}S - \int_S H_{ijk}(P,Q) u_k(Q)\, \mathrm{d}S, \tag{5}$$

where

$$G_{ijk}(P,Q)=\tfrac{1}{2}C_{ijln}(U_{lk,n}(P,Q)+U_{nk,l}(P,Q)),$$
$$H_{ijk}(P,Q)=\tfrac{1}{2}C_{ijln}(T_{lk,n}(P,Q)+T_{nk,l}(P,Q)). \tag{6}$$

Both Eqs. (4) and (5) can be written as a fast numerical sum over: quadrature points ($1\leqslant n,s\leqslant N_{\text{Gauss}}$) associated with weight factors (w_n and w_s), number of nodes per boundary element ($1\leqslant c\leqslant N_n$) and number of boundary elements ($1\leqslant m\leqslant N_e$). For instance, Eq. (5) would be in the form

$$\sigma_{ij}(P)=\sum_{m=1}^{N_e}\sum_{c=1}^{N_n}\sum_{n=1}^{N_{\text{Gauss}}}\sum_{s=1}^{N_{\text{Gauss}}}w_nw_sG_{kij}(P,Q)N_c(x_1,x_2)J(x_1,x_2)t_k(Q)$$
$$-\sum_{m=1}^{N_e}\sum_{c=1}^{N_n}\sum_{n=1}^{N_{\text{Gauss}}}\sum_{s=1}^{N_{\text{Gauss}}}w_nw_sH_{kij}(P,Q)N_c(x_1,x_2)J(x_1,x_2)u_k(Q), \tag{7}$$

where the functions $N_c(x_1,x_2)$ are quadratic shape functions and the Jacobian of transformation J is equal to $\sqrt{\mathrm{d}x_1^2+\mathrm{d}x_2^2}$. This fast sum equation (7) is used to calculate the stresses at all dislocation nodes and is added to the infinite medium solution given by Eq. (2).

Comparing the structure of Eqs. (2) and (7), one can easily note the great degree of similarity and consistency between the PDD formation (Eq. (2)) and the BEM formulation (Eq. (7)). In the PDD, the fast sums are carried over quadrature points and the number of segments on each dislocation and the outer summation is over the number of dislocation loops, while the sums in the BEM are carried over the number of quadrature points twice and the number of nodes per element and the outer summation is finally performed over the number of surface elements. Thus, the computational structure of both the PDD and the BEM is essentially the same. It is therefore convenient to model the effects of surface image forces with the BEM, while the computational structure of the PDD is unchanged. One possible additional advantage of this computational structure is the suitability of incorporating acceleration algorithms of conventional particle methods, and as the Greengard–Rokhlin (1987) fast multi-pole algorithms.

Once the dislocation stress field and the image stress field are obtained the total stress and hence the total force on each dislocation can be computed and the evolution of the microstructure can be obtained using the framework of the PDD method.

3. Accuracy and convergence of the method

To determine the accuracy of the numerical method, and to show that the method is numerically convergent, we will consider two ideal cases with known "limiting" analytical solutions.

3.1. Case 1: screw dislocation parallel to a free surface

Consider a screw dislocation parallel to a free surface of a finite body, and located at a distance l away from the surface. The exact solution can be obtained by a simple image construction (Hirth and Lothe, 1982). Thus, the free surface condition (zero traction) can be achieved through the superposition of the stress field of the original screw dislocation with that of an imaginary (image screw dislocation) of the same strength and of opposite sign located at a mirror position on the other side of the free surface. The screw dislocation is drawn towards the surface by a normalized image force equal to

$$\frac{\widetilde{F}}{\widetilde{b}}=-\frac{\widetilde{b}}{4\pi\widetilde{l}}, \tag{8}$$

where $\widetilde{F}=F/(\mu La)$ is the dimensionless force/unit length on a screw dislocation of length L, $\widetilde{b}=b/a$ is the dimensionless magnitude of the Burgers vector, $\widetilde{l}=l/a$ is the dimensionless distance, and a is the lattice parameter. To test the present numerical method, we approximate the infinite screw dislocation by a "very long" segment, 18,000 in length (note that all distances henceforth are dimensionless). Fig. 1a shows the

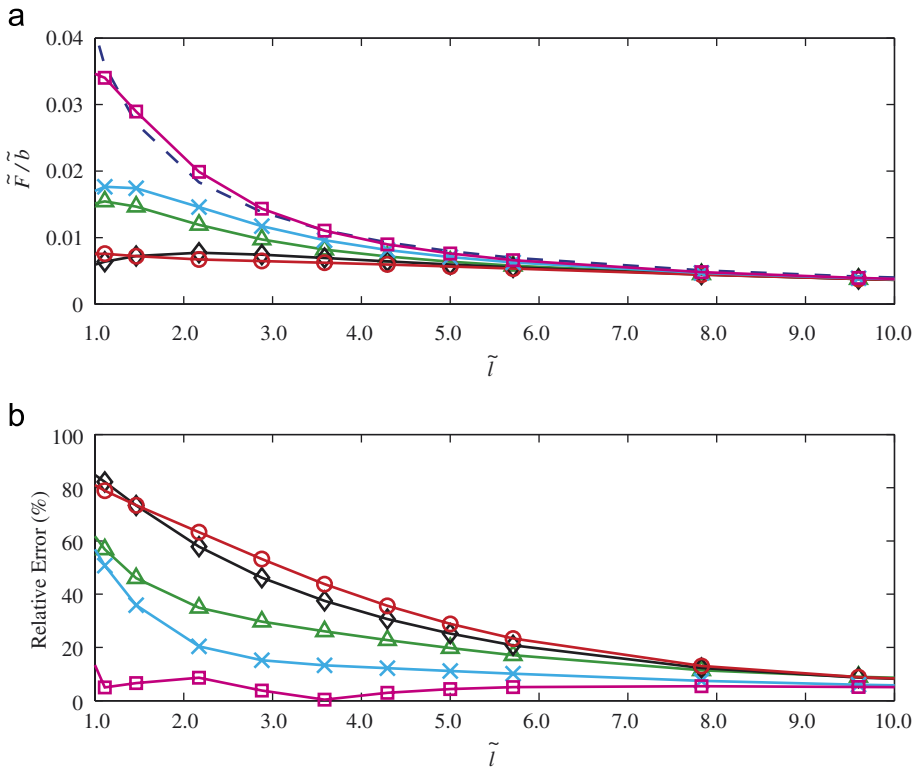

Fig. 1. (a) Normalized image force on the screw dislocation (the dashed curve is the analytical solution) versus distance from free surface; (b) variation of the corresponding relative error with distance from the free surface. The number of quadrature points are kept at 16, while the surface mesh density is varied: (−o−) 6 × 6 elements, (−◇−) 8 × 8 elements, (−△−) 10 × 10 elements, (− × −) 12 × 12 elements, and (−□−) 20 × 10 elements.

normalized image force calculated using the PDD-BEM method on the screw dislocation, placed at various distances from the free surface. The image force as predicted by the analytical solution given by Eq. (8) is also shown in Fig. 1a. The dislocation is divided into 90 segments, with 16 quadrature points per segment. The free surface parallel to the screw dislocation is represented by a surface mesh extending over the dimensions $20,000 \times 20,000$. The corresponding relative error between the solution from the PDD-BEM method and the analytical solution is shown in Fig. 1b.

To determine the convergence rate of the numerical solution and the dependence of the relative error on the discretization procedure, we increase the number of quadrature integration points on each dislocation segment to 64 in Fig. 2a, and to 128 in Fig. 2b. The figures display the relative error in the numerical solution (taking the analytical solution again as a reference). It is clear from these figures that the error converges as the number of quadrature points is increased. Also, the errors decrease rapidly with increasing the number of quadrature points, especially as the dislocation gets closer to the free surface. When the dislocation is relatively far from the free surface (e.g. at distances $\tilde{l} \gg 10$), the error in image force calculations can be kept below a few percent with a relatively small number of quadrature points on each segment (e.g. 16). However, when the dislocation is at a distance, $\tilde{l} < 10$ from the surface, the number of quadrature points needs to be significantly increased to attain the same level of relative error.

3.2. Case 2: cylinder containing a coaxial screw dislocation

Consider a finite cylinder that has a coaxial screw dislocation. Due to the finite length of the cylinder, the coaxial screw dislocation will cause the cylinder to twist. Eshelby (1953) worked out an analytical solution and predicted that two cross-sections of a cylinder containing a coaxial dislocation, will undergo a relative

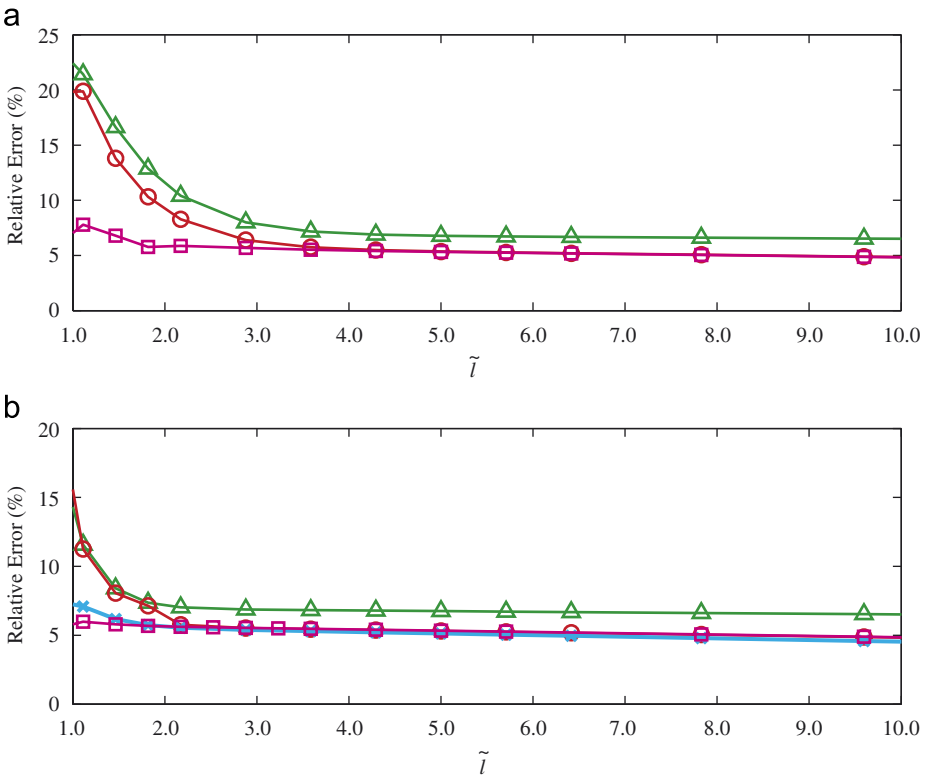

Fig. 2. (a) Relative error in the calculated image force for 64 quadrature points versus distance from free surface; (b) variation of the relative error in the calculated image force for 128 quadrature points with distance from the free surface. The surface mesh density is varied as follows: (−△−) 6 × 6 elements, (–o–) 10 × 10 elements, (− × −) 12 × 12 elements, and (−□−) 20 × 10 elements.

rotation angle θ, given by

$$\theta = \frac{\widetilde{b}\widetilde{L}}{\pi \widetilde{R}^2}, \tag{9}$$

where $\widetilde{L} = L/a$ is the dimensionless distance between the two cross-sections, and $\widetilde{R} = R/a$ is the dimensionless radius of the cylinder. This is the so-called Eshelby twist. According to St. Venant's principle, this elementary result can only be used at distances greater than $2\widetilde{R}$ from the ends.

Here the accuracy and convergence of the PDD-BEM is investigated by computing the deformed shape of a cylinder containing a coaxial screw dislocation and comparing the results to the analytical solution given by Eq. (9). Consider a cylinder of radius $\widetilde{R} = 500$ and length to diameter ratio of 5:1. Fig. 3a shows the surface mesh for the cylinder free of dislocations. Adding a coaxial screw dislocation to the cylinder and using the PDD-BEM method we obtain the deformed configuration shown in Fig. 3b. It is observed from the results that u_z, the z-component of the displacement, is discontinuous across the plane defined by $y = 0, x > 0$ with

$$\lim_{\varepsilon \to 0, x>0} [u_z(x, -\varepsilon) - u_z(x, \varepsilon)] = b_z, \tag{10}$$

where for the current analysis $b_z = 0.5$ and the dimensionless Burgers vector is equal to $\widetilde{b} = (0, 0, b_z)$. In addition, the cylinder twists due to the presence of the coaxial screw dislocation. To predict the accuracy of the PDD-BEM results, the relative twist angle between two cross-sections of the cylinder is compared to the analytical Eshelby twist given by Eq. (9). The two cross-sections are chosen, in accordance with St. Venant's principle, to be located at distances $3\widetilde{R}$ and $4\widetilde{R}$ from the bottom edge, respectively.

The relative error of the twist angle, for different numbers of surface elements is shown in Fig. 4. For these results, the screw dislocation is divided into 30 segments with 16 quadrature points per segment. It is clear that increasing the number of elements, either on the sides of the cylinder or on the top and bottom planes, will

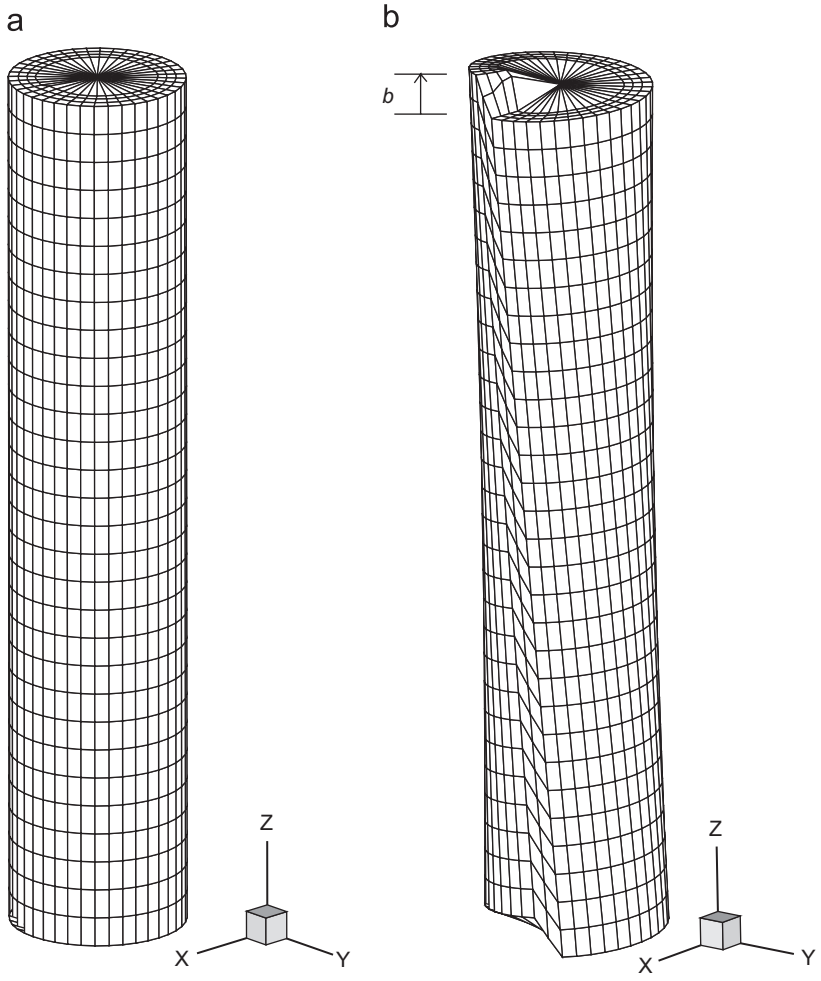

Fig. 3. (a) Dislocation free cylinder. (b) Deformed shape of the cylinder containing a coaxial screw dislocation as predicted from the PDD-BEM method.

decrease the relative error in the twist angle. One factor to be considered here is that the numerical method itself is an approximation of the "infinitely long" cylinder assumption of Eshelby, and hence only relative rates of convergence can be ascertained by comparing with the reference analytic solution of Eshelby. In addition, the screw dislocation in our model ends on the top and bottom surfaces. This means that some segments are less than a few lattice parameters from the surface. Thus, as was discussed in case 1, one can decrease the relative error in the calculated image forces on these segments, and therefore the relative error in the twist angle, by increasing the number of quadrature points on such segments.

4. 3-D simulations of single-slip behavior in cylindrical microcrystals

Recently, compression experiments were carried out to study the crystal-size dependence and the behavior of single-crystal micropillars (Uchic et al., 2004; Greer et al., 2005; Dimiduk et al., 2005; Uchic and Dimiduk, 2005). These characterized experiments can be used to guide the development of predictive plasticity models. In addition, a number of 2-D and 3-D DDD models have been utilized to study the size-effect dependence of micropillars (Deshpande et al., 2005; Benzerga and Shaver, 2006; Tang et al., 2007). It is noted that in 2-D dislocation dynamic methods (Deshpande et al., 2005; Benzerga and Shaver, 2006), key dislocation interaction mechanisms are either neglected or added in an ad hoc manner. We wish to show here that, in contrast to 3-D models that ignore surface effects (Tang et al., 2007), image fields arising from the finite geometry of

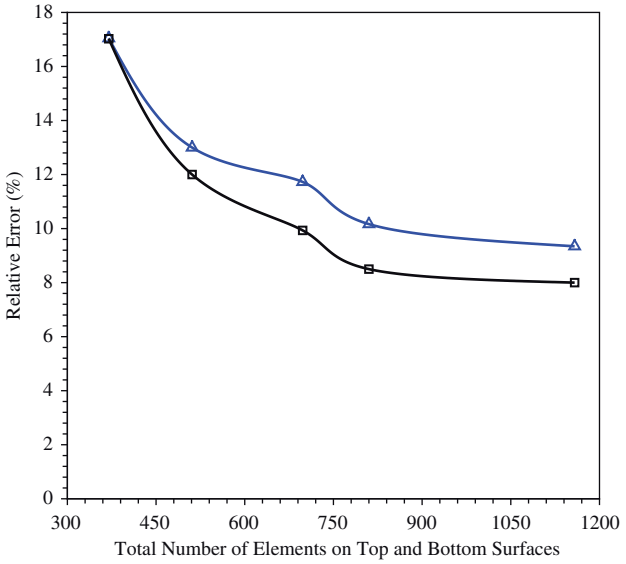

Fig. 4. Relative error in the twist between two cross-sections of a cylinder, located at $3\widetilde{R}$ and $4\widetilde{R}$ from the bottom surface, respectively, for different numbers of surface elements. The side surface mesh density is varied as follows: (−△−) 800 elements and (−□−) 1200 elements.

micropillars have an important effect on the dislocation microstructure, especially for micropillars having submicron diameters.

We utilize here the PDD-BEM method to study the single-slip behavior of cylindrical microcrystals. In the following, we perform large scale 3-D dislocation simulations of the experiments performed by Dimiduk et al. (2005). In the following subsections, the problem setup and the simulation results are presented and discussed.

4.1. Problem setup

For comparison between simulation results and existing experimental conditions, the problem setup is chosen to represent the recent experiments of Dimiduk et al. (2005). Fig. 5 shows a schematic of a face-centered-cubic (FCC) single-crystal micropillar used in the current simulations. A uniform compressive load in the z direction is imposed on the top surface of the cylinder while the bottom surface is kept fixed.

Experimental observations of Au single-crystal micropillars under compression (Volkert and Lilleodden, 2006) revealed that the resultant stress–strain behavior did not depend on whether single or multiple slip occurs. Thus, although the loading direction in our simulation would activate multi-slip-systems, we assume in this work that the single crystal will have the slip-system $\langle 0\,1\,1\rangle$ $(1\,1\,1)$ as the only activated slip system. This assumption may be justified if one considers the low dislocation densities typical of these systems at small plastic strains. Certainly at higher dislocation densities, one would expect the activation of multiple slip as a result of the abundance of cross-slip events.

Crystal properties are taken to be that of nickel with a shear modulus $\mu = 76\,\text{GPa}$, Poisson's ratio $v = 0.31$, lattice parameter $a = 3.524\,\text{Å}$, and Burgers vector magnitude of $b = 0.25\,\text{nm}$. In addition, the aspect ratio of the cylinder is fixed at $L{:}D = 3{:}1$ in all current simulations. The spacing between activated slip planes is generated at random such that all planes remain in the slip zone defined as shown in Fig. 5. Compression loading is performed under a constant strain rate $\dot{\varepsilon} = 200\,\text{s}^{-1}$. Thus, the rate of loading is set by this strain rate such that

$$\dot{\sigma} = E(\dot{\varepsilon} - \dot{\varepsilon}^{\text{p}}), \tag{11}$$

where E is the elastic modulus of the material and $\dot{\varepsilon}^{\text{p}}$ is the plastic strain rate that is obtained from the motion of the dislocations as follows:

$$\dot{\varepsilon}^{\text{p}} = -\frac{1}{2V}\sum_{i=1}^{N_{\text{tot}}} l_i v_i(\mathbf{n}_i \otimes \mathbf{b}_i + \mathbf{b}_i \otimes \mathbf{n}_i), \tag{12}$$

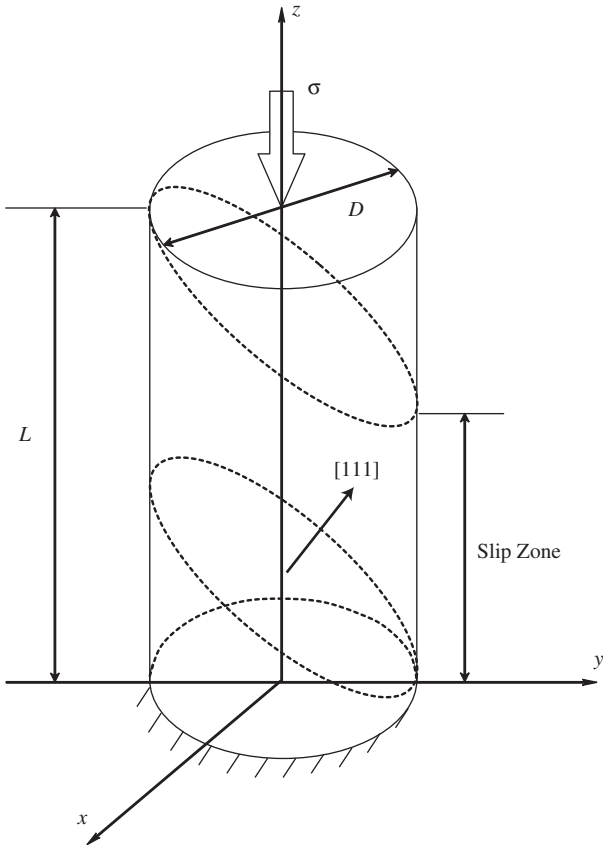

Fig. 5. Schematic of an FCC single-crystal micropillar oriented for single-slip. The micropillar is imposed by axial compression along the [0 0 1] axis. In all simulations, the slip zone is confined as shown.

where V is the volume of the simulated crystal and N_{tot} is the total number of dislocation segments. In addition, l_i is the length of dislocation segment i having a velocity magnitude v_i, a Burgers vector $\mathbf{b}_i$, and a slip plane normal $\mathbf{n}_i$.

4.2. Results and discussion

To gain insight into the effects of micropillar size on dislocation microstructure evolution, a statistical analysis was performed on two distinct micropillar sizes having diameters $D = 1.0$ and $0.5\,\mu\text{m}$, respectively. For each of the two micropillar sizes, 10 different samples having a statistical variation of the initial microstructure were studied.

The initial microstructure in our current analysis is constructed by randomly distributing Frank–Read (FR) sources in the bulk of the crystal. The FR source length to the crystal diameter, λ/D, is treated as a uniformly random variable. The distribution was chosen to be a uniform distribution such that ($\lambda_{\min} \leqslant \lambda \leqslant D$), where clearly the maximum FR source length, $\lambda_{\max}$, is bounded by the diameter of the crystal, and the minimum dislocation length was chosen to be 20 nm.

In our estimate of the minimum FR source length, we utilized the experimentally measured maximum strength to determine an approximate value for the resolved shear stress on the slip plane. The Schmidt factor for the slip system we have chosen is about 0.408 and we determined from approximate Orowan-type calculations that the critical resolved shear stress for an FR source having a length $\lambda_{\min} = 20\,\text{nm}$ is about 1.0 GPa. Thus the maximum applied stress needed to activate an FR source that has this critical resolved shear stress would be 2.45 GPa. This value is several times larger than the maximum flow stress reached in the

experiments of Dimiduk et al. (2005), which is 400 MPa for a micropillar having $D = 1.0\,\mu m$. Thus, we know that although FR sources that might have a higher critical resolved shear stress (i.e. having a length smaller than λ_{min}) may exist in the crystal, such small pinned dislocation segments will not be activated under the current conditions.

The engineering stress–strain curves resulting from the simulations of all 10 samples of the two micropillars are shown in Fig. 6. The initial dislocation density in all simulations are in the range $1.6 \times 10^{12} \leqslant \rho \leqslant 4 \times 10^{12}\,m^{-2}$, in agreement with densities reported by Dimiduk et al. (2005). A summary of the initial mean dislocation source length, the standard deviation, and the computed flow stresses for all simulated cases are shown in Table 1.

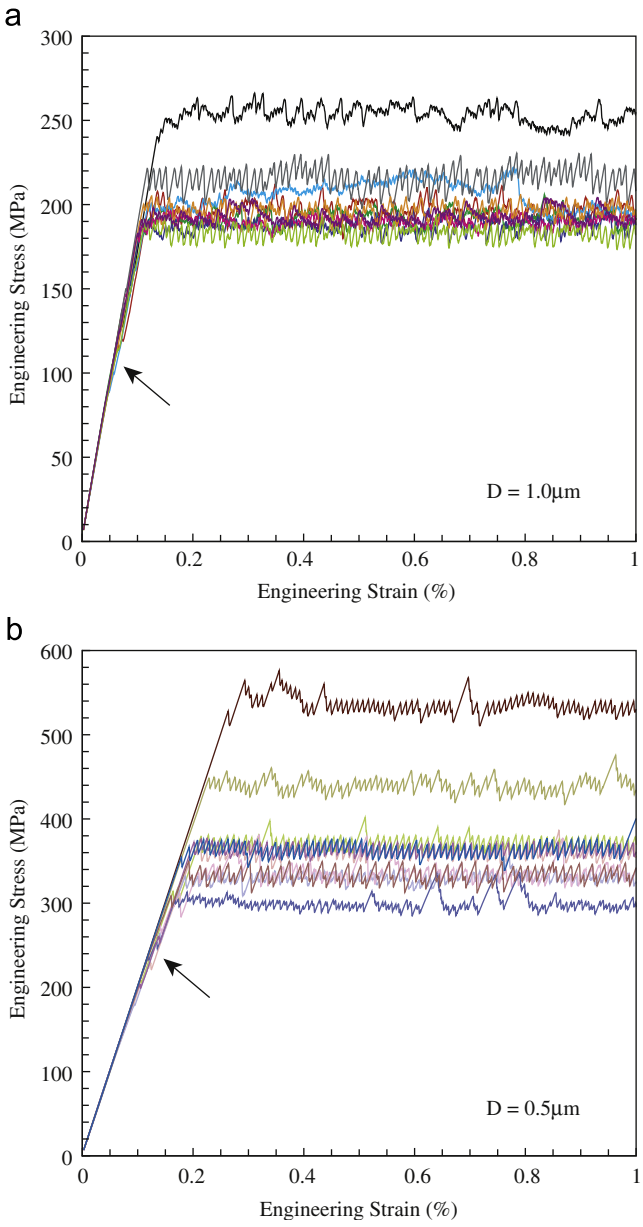

Fig. 6. Statistical results of the engineering-stress versus engineering-strain curves for two different samples having an aspect ratio of 3:1 and diameters: (a) $D = 1.0\,\mu m$ and (b) $D = 0.5\,\mu m$. The arrows point to step formation in the elastic region for some of the samples.

Table 1
Summary of parameters for $D = 1.0$ and $0.5\,\mu m$

Case #	$D = 1.0\,\mu m$			$D = 0.5\,\mu m$		
	Mean source length (μm)	Standard deviation (μm)	Flow stress (MPa)	Mean source length (μm)	Standard deviation (μm)	Flow stress (MPa)
1	0.55	0.28	251	0.16	0.02	535
2	0.62	0.25	201	0.25	0.04	361
3	0.70	0.18	202	0.24	0.09	370
4	0.63	0.31	207	0.20	0.12	330
5	0.57	0.29	189	0.28	0.06	330
6	0.45	0.25	192	0.28	0.03	437
7	0.39	0.30	218	0.26	0.05	304
8	0.51	0.32	196	0.32	0.09	364
9	0.60	0.21	186	0.22	0.04	333
10	0.42	0.31	189	0.09	0.08	362

The influence of the micropillar size on the stress–strain behavior and the flow stress is clearly shown in Fig. 6. The flow stress increases as the size of the sample decreases, and after the flow stress is reached, essentially no work hardening is observed. Another interesting feature revealed here is the initiation of strain bursts observed in the elastic region of some of the samples, as indicated by the arrows in Fig. 6. All these features are in agreement with experimental observations (Dimiduk et al., 2005; Greer et al., 2005).

To understand the mechanisms under which such observations occur, a detailed study of the dislocation microstructure evolution for all the simulated samples was made. Fig. 7 shows the engineering stress–engineering strain curve and the microstructure evolution for the micropillar with diameter $D = 1.0\,\mu m$. The initial dislocation density is $\rho = 2.35 \times 10^{12}\,m^{-2}$, the FR source mean length is $0.55\,\mu m$ and the standard deviation is $0.28\,\mu m$ (case 1 in Table 1). The surface mesh and the micropillar geometry before deformation is shown in Fig. 8a.

As the load on the micropillar increases beyond an initial threshold, larger size FR sources start expanding rapidly in the bulk until they interact with the free surface. This results in the termination of the dislocation at the crystal surface, splitting it into two segments that are pinned only at one end in the bulk while the other end is free to move on the surface. These singly pinned dislocations, depending on the length as well as the closeness of the original FR source to the surface, will in general have a different length from that of the FR source. If the length of these single-ended dislocations is smaller than the initial FR source, and the resolved shear stress did not reach the critical threshold required for it to continue propagating, then these segments will get stuck near the surface (Figs. 7b–e). When the strain reaches 0.13%, all larger sources will have interacted with the surface (i.e. exhausted) and produced shorter segments that need a higher resolved shear stress to break away from the surface. The initial expansion and interaction with the free surface of these larger segments is observed as a strain burst on the stress–strain curve. Afterwards, the loading increases elastically until the resolved shear stress on the largest segment exceeds its threshold value, and it breaks away from the surface (Fig. 7e). The motion of this dislocation will proceed as long as it does not encounter any other obstacle (Figs. 7f and g). This is observed on the stress–strain curve as a rapid continuous strain burst and, in addition, the micropillar will slip and deform continuously. The deformed shape of the micropillar after 2% strain is shown in Fig. 8b and is in agreement with the deformed shapes observed experimentally by Dimiduk et al. (2005) on $1.0\,\mu m$ micropillars.

It should be noted that, as FR sources expand and intersect the surface, the resulting single-ended dislocations will have a length distribution of $(0 \leqslant \lambda \leqslant D - \lambda_{min})$. Since this resulting distribution is somewhat similar to the initial FR source distribution and since the stress–strain response is an integrated process of many stochastic events, the influence of the location of the initial end points on the stress–strain behavior is minimal.

In addition, as the strain increases and the cylinder slips the length of singly pinned dislocations on the slipped plane will change which may result in trapping previously activated dislocations or may lead to the

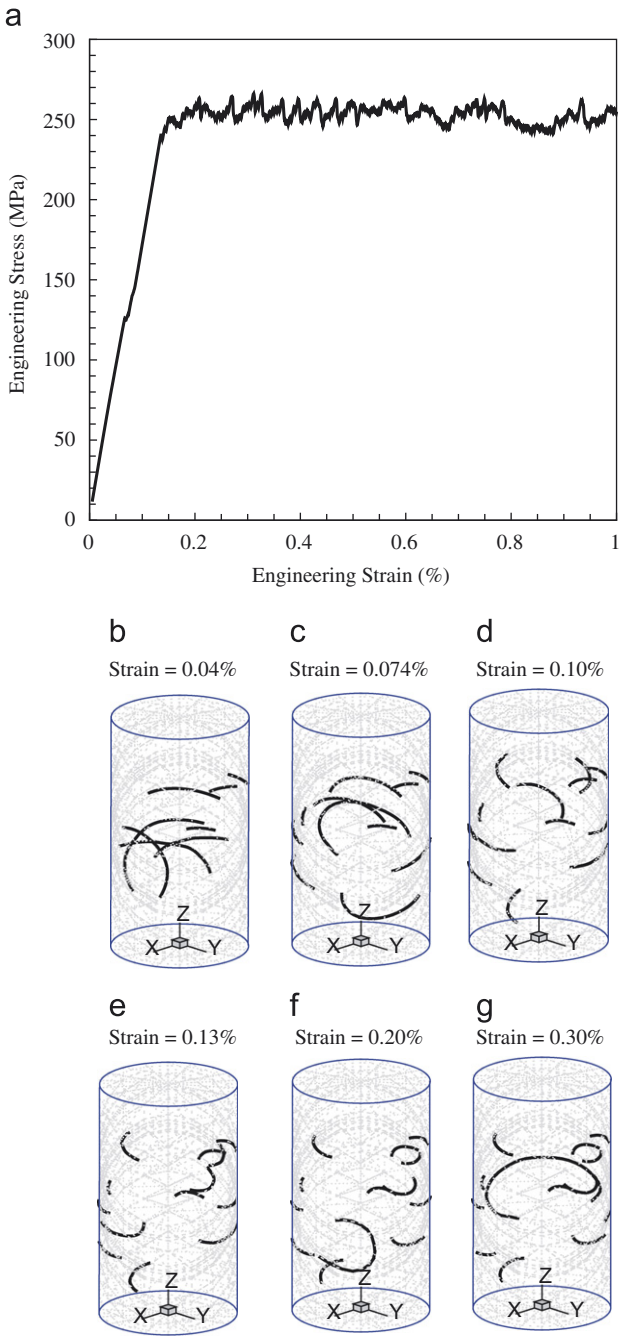

Fig. 7. (a) Engineering stress–engineering strain curve for the micropillar and (b)–(g) the microstructure evolution at different strains. The micropillar has an aspect ratio of 3:1 and diameter $D = 1.0\,\mu m$. The initial dislocation density is $\rho = 2.35 \times 10^{12}\,m^{-2}$, FR source mean length is 0.55 μm and the standard deviation is 0.28 μm.

activation of other sources. When the slipping of the micropillar results in trapping of previously activated dislocations, the loading will increase elastically until the threshold stress on the dislocation segment with the lowest critical resolved shear stress is reached and thus it will break away from the surface and the process continues in a similar manner as discussed previously.

Such microstructure evolution was observed in all samples simulated for both the 1.0 and the 0.5 μm diameter micropillars. The difference between both sizes was observed to be in the length of the single-ended

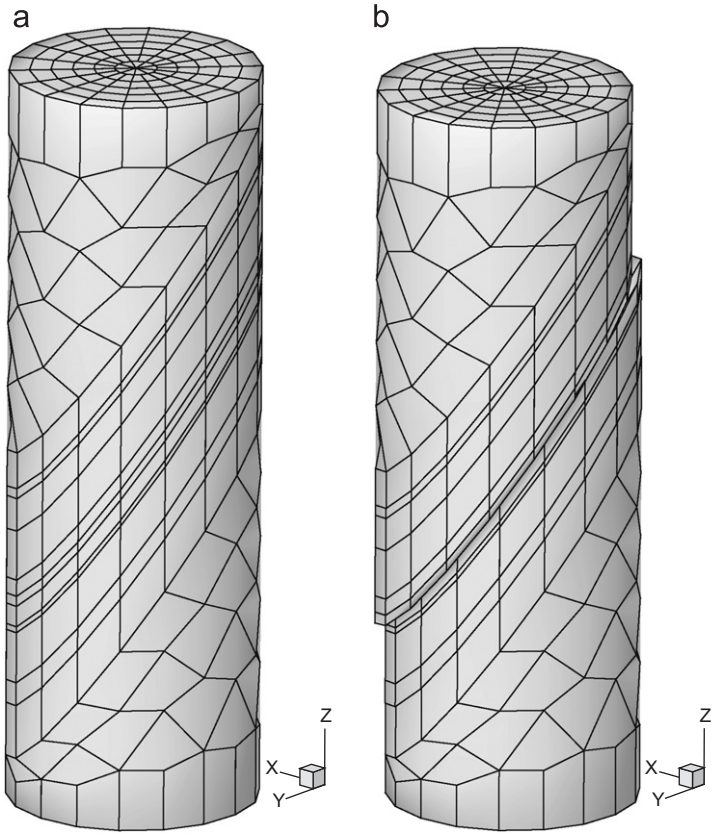

Fig. 8. The 1.0 μm diameter micropillar (a) before and (b) after deformation (2% strain). The surface mesh is shown. The initial dislocation density is $\rho = 2.35 \times 10^{12}\,\mathrm{m}^{-2}$.

dislocations trapped at the surface. When the size of the micropillar decreases, the length of the FR sources will be closer to the size of the micropillar and thus after it expands it will get trapped at the surface with a smaller length than in the case of micropillars with larger sizes. Thus, these single-ended surface dislocations will need a higher stress to be activated.

The flow stress for all simulated cases versus the square root of the dislocation density in the cylinder at the onset of plastic flow is shown in Fig. 9 for micropillar with diameters 1.0 and 0.5 μm, respectively. For both sizes the behavior is observed to be distinct from that of bulk crystals. A decrease in the flow stress is observed as the square root of the dislocation density increases. This indicates that for small size micropillars, the flow stress is not controlled by dislocation–dislocation interaction as in the case of bulk crystals, but is controlled by the activation of the weakest dislocation link trapped at the surface. This can be observed from Fig. 10, where the flow stress is plotted against the inverse mean dislocation length at the onset of plastic flow (normalized to the cylinder diameter).

It is clearly seen that the mean length of trapped dislocations on the surface of the crystal is the dominant factor influencing the size effect on the strength. It is thus possible to rationalize the experimentally observed size effects based on a statistical variation of the single-ended dislocation source lengths. This supports similar findings reported by Parthasarathy et al. (2007).

In almost all DD simulations so far, image force effects on microstructure evolution and the flow stress were neglected. It has been argued that the neglect of image field in 3-D dislocation dynamics allows numerical efficiency without compromising accuracy. To asses the importance (or lack thereof) of accurately including the image field of dislocations in DD simulations, three different micropillar sizes having diameters $D = 1.0, 0.5$, and $0.15\,\mu\mathrm{m}$ were studied. For each size, two simulations were carried out; one that includes the image field as calculated from the BEM-PDD discussed above, and the other ignores the image field totally.

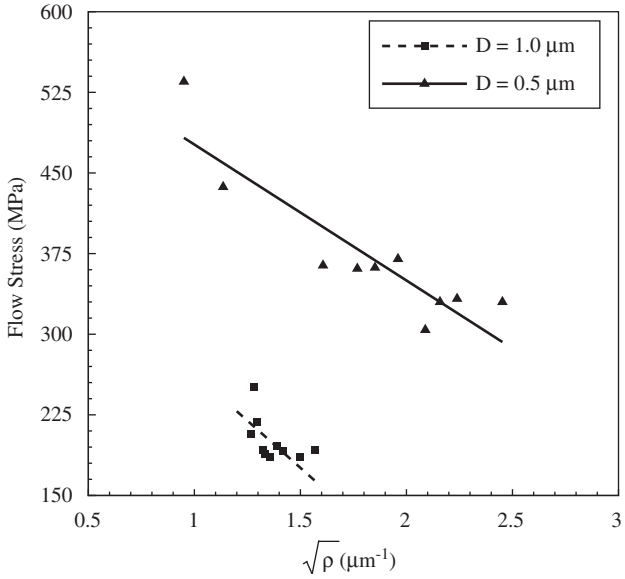

Fig. 9. The flow stress versus the square root of the dislocation density at the onset of plastic flow for the 1.0 and the 0.5 μm micropillars.

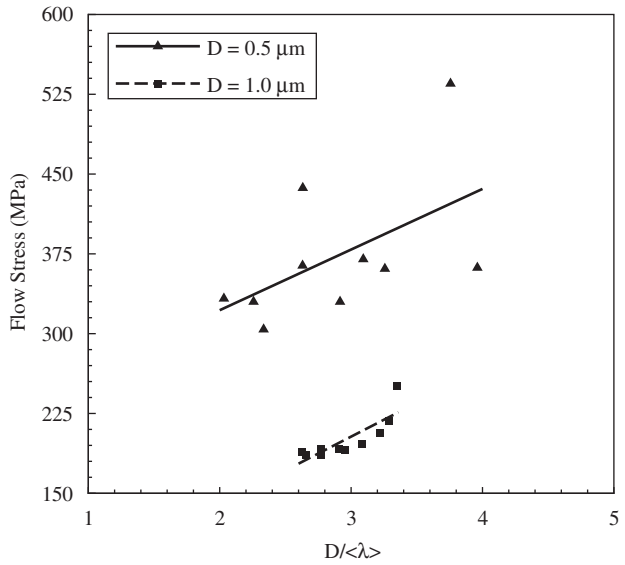

Fig. 10. Flow stress versus the inverse mean dislocation length (normalized to the cylinder diameter) at the onset of plastic flow for the 1.0 and the 0.5 μm micropillars.

The relative difference in the calculated flow stress between both cases as a function of the micropillar diameter is plotted in Fig. 11.

The image field is observed to affect the microstructure by assisting trapped dislocations in breaking away from the surface. Thus the flow stress when considering the image field is lowered by the percentages shown in Fig. 11 from the calculated flow stress when we ignore the image field. The relative difference is calculated to be 10.05% for the micropillar with diameter $D = 1.0\,\mu m$ and increases as the micropillar diameter decreases. The relative difference is 18.39% for the micropillar with diameter $D = 0.15\,\mu m$. This is due to the fact that for smaller sizes the surface to volume ratio is larger and thus the image field on the dislocations will be higher

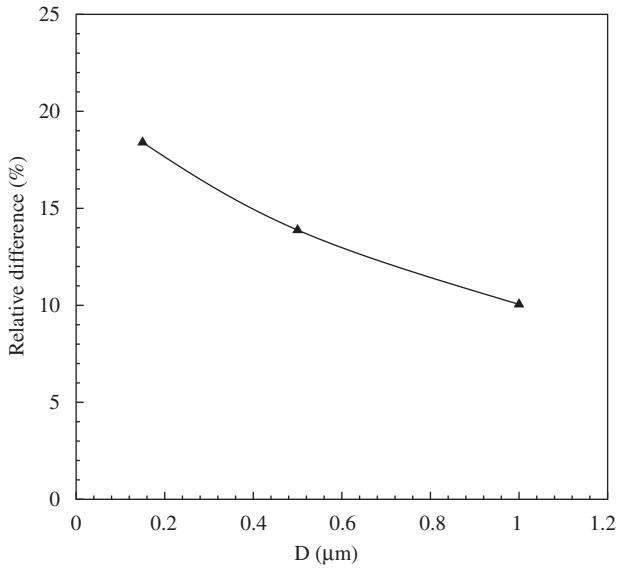

Fig. 11. The relative difference in the calculated flow stress between DD simulations with and without surface image fields.

than in the case of larger sizes where the image field is weaker. Thus, for micropillars having large diameters (greater than 1.0 μm) the effect of the image field may be neglected with small errors, while as the diameter of the sample decreases to the submicron range, the effect of the image field becomes substantial and can no longer be neglected.

5. Conclusions and discussion

A self-consistent boundary element-dislocation dynamics framework has been established to critically examine the influence of free surfaces on dislocation motion. By considering special cases for which analytical solutions are known, it is shown that the method is very accurate for calculating surface image forces on dislocations. By increasing the surface mesh density for BEM calculations, and the quadrature point density on dislocation segments, it is shown that the error can be controllably made to be small, and that the numerical solution displays absolute convergence.

As an application of the current method, the PDD-BEM was utilized to study the size effects and the single-slip behavior of cylindrical microcrystals through a large scale 3-D dislocation simulations that mimics the experimental conditions of Dimiduk et al. (2005). The size effects on the flow stress are clearly observed and the results are in complete agreement with experimental observations. By a thorough study of the microstructure evolution the observed size effects were rationalized based on a statistical variation of the length of single-ended dislocation sources in the crystal.

The effect of the image field on the results was shown to increase as the diameter of the micropillar decreases or as the surface to the volume ratio of the cylinder increases. For larger diameters the image field can be neglected with small errors, but as the dimensions get smaller (in the range of submicrons) the effect of the image forces becomes substantial and cannot be neglected.

Finally, it should be noticed that the BEM formulation presented here can be extended to inhomogeneous materials or problems with rigid inclusions (e.g. precipitate surfaces) with the use of established techniques as shown by Takahashi and Ghoniem (2007). Thus, coupling between such methods and the current method can be utilized to model and study the size-effect dependence of micropillar superalloys presented by Uchic et al. (2004). In addition, our current method can be extended to any system (isotropic or anisotropic) consisting of any number of materials, where rigid, sliding or friction conditions are imposed at interfaces without difficulty.

Acknowledgments

We acknowledge the support of the US Air Force Office for Scientific Research (AFOSR), through Grant no. FA9550-07-1-0396, with UCLA. S.B. Biner was supported by DOE under contract W-7505-Eng with Iowa State University, and by the Director of Energy Research, Office of Basic Sciences.

References

Arzt, E., Dehm, G., Gumbsch, P., Kraft, O., Weiss, D., 2001. Interface controlled plasticity in metals: dispersion hardening and thin film deformation. Prog. Mater. Sci. 46 (3–4), 283–307.

Basinski, Z.S., Pascual, R., Basinski, S.J., 1983. Low amplitude fatigue of copper single crystals-I. The role of the surface in fatigue failure. Acta Metall. 31 (4), 591–602.

Becker, A., 1992. The Boundary Element Method in Engineering. McGraw-Hill International, London, UK.

Benzerga, A.A., Shaver, N.F., 2006. Scale dependence of mechanical properties of single crystals under uniform deformation. Scr. Mater. 54 (11), 1937–1941.

Deshpande, V.S., Needleman, A., Van der Giessen, E., 2005. Plasticity size effects in tension and compression of single crystals. J. Mech. Phys. Solids 53 (12), 2661–2691.

Dimiduk, D.M., Uchic, M.D., Parthasarathy, T.A., 2005. Size-affected single-slip behavior of pure nickel microcrystals. Acta Mater. 53 (15), 4065–4077.

Eshelby, J.D., 1953. Screw dislocation in thin rods. J. Appl. Phys. 24 (24), 176–179.

Fivel, M.C., Gosling, T.J., Canova, G.R., 1996. Implementing image stresses in a 3d dislocation simulation. Modeling Simulation Mater. Sci. Eng. 4 (6), 581–596.

Ghoniem, N.M., Sun, L.Z., 1999. Fast sum method for the elastic field of 3-d dislocation ensembles. Phys. Rev. B 60 (1), 128–140.

Ghoniem, N.M., Tong, S.-H., Sun, L.Z., 2000. Parametric dislocation dynamics: a thermodynamics-based approach to investigations of mesoscopic plastic deformation. Phys. Rev. B 61 (2), 913–927.

Gosling, T.J., Willis, J.R., 1994. A line-integral representation for the stresses due to an arbitrary dislocation in an isotropic half-space. J. Mech. Phys. Solids 42 (8), 1199–1221.

Greengard, L., Rokhlin, V., 1987. A fast algorithm for particle simulations. J. Comput. Phys. 73 (2), 325–348.

Greer, J.R., Oliver, W.C., Nix, W.D., 2005. Size dependence of mechanical properties of gold at the micron scale in the absence of strain gradients. Acta Mater. 53 (6), 1821–1830.

Hirth, J.P., Lothe, J., 1982. Theory of Dislocations, second ed. Wiley, New York.

Khraishi, T.A., Zibib, H.M., de la Rubia, T.D., 2001. The treatment of traction-free boundary condition in three-dimensional dislocation dynamics using generalized image stress analysis. Mater. Sci. Eng. A 309–310, 283–287.

Kubin, L.P., Canova, G., Condat, M., Devincre, B., Pontikis, V., Brechet, Y., 1992. Dislocation microstructures and plastic flow: a 3D simulation. Diffusion and Defect Data—Solid State Data, Part B (Solid State Phenomena) 23–24, 455.

Kukta, R.V., Freund, L.B., 1998. Three-dimensional numerical simulation of interacting dislocations in a strained epitaxial surface layer. In: Bulatov, V., de la Rubia, T.D., Phillips, R., Kaxiras, E., Ghoniem, N. (Eds.), Multiscale Modelling of Materials, Materials Research Society Symposium Proceedings, vol. 538. Materials Research Society, pp. 99–105.

Lothe, J., Indenbom, V., Chamrov, V., 1982. Elastic field and self-force of dislocations emerging at the free surfaces of an anistropic halfspace. Phys. Stat. Solidi (b) 11, 671–677.

Martinez, R., Ghoniem, N.M., 2002. The influence of crystal surfaces on dislocation interactions in mesoscopic plasticity: a combined dislocation dynamics—finite element approach. J. Comput. Mater. Science 3 (2), 229–243.

Mughrabi, H., 1992. Introduction to the viewpoint set on: surface effects in cyclic deformation and fatigue. Scr. Metall. Mater. 26 (10), 1499–1504.

Parthasarathy, T.A., Rao, S.I., Dimiduk, D.M., Uchic, M.D., Trinkle, D.R., 2007. Contribution to size effect of yield strength from the stochastics of dislocation source lengths in finite samples. Scr. Mater. 56 (4), 313–316.

Schwarz, K.W., 1999. Simulation of dislocations on the mesoscopic scale. J. Appl. Phys. 85 (1), 108–129.

Takahashi, A., Ghoniem, N.M., 2007. A computational method for dislocation–precipitate interaction. J. Mech. Phys. Solids, in press, doi:10.1016/j.jmps.2007.08.002.

Tang, H., Schwarz, K.W., Espinosa, H.D., 2007. Dislocation escape-related size effects in single-crystal micropillars under uniaxial compression. Acta Mater. 55 (5), 1607–1616.

Uchic, M., Dimiduk, D., Florando, J., Nix, W., 2004. Sample dimensions influence strength and crystal plasticity. Science 305, 986–989.

Uchic, M.D., Dimiduk, D.M., 2005. A methodology to investigate size scale effects in crystalline plasticity using uniaxial compression testing. Mater. Sci. Eng. A 400–401, 268–278.

Van der Giessen, E., Needleman, A., 1995. Discrete dislocation plasticity: a simple planar model. Modeling Simulation Mater. Sci. Eng. 3 (5), 689–735.

Verdier, M., Fivel, M., Groma, I., 1998. Mesoscopic scale simulation of dislocation dynamics in fcc metals: principles and applications. Modeling Simulation Mater. Sci. Eng. 6 (6), 755–770.

Volkert, C.A., Lilleodden, E.T., 2006. Size effects in the deformation of sub-micron Au columns. Philos. Mag. 86 (33–35), 5567–5579.

von Blanckenhagen, B., Gumbsch, P., Arzt, E., 2001. Dislocation sources in discrete dislocation simulations of thin-film plasticity and the Hall-Petch relation. Modelling Simulation Mater. Sci. Eng. 9 (3), 157–169.

Weygand, D., Friedman, L.H., Van der Giessen, E., Needleman, A., 2002. Aspects of boundary-value problem solutions with three-dimensional dislocation dynamics. Modeling Simulation Mater. Sci. Eng. 10 (4), 437–468.

Zbib, H.M., Rhee, M., Hirth, J.P., 1998. On plastic deformation and the dynamics of 3d dislocations. Int. J. Mech. Sci. 40 (2–3), 113–127.